A Retrofit Capacitive Sensing Occupancy Detector Using Fluorescent Lamps

John J. Cooley, *Student Member, IEEE*, Al-Thaddeus Avestruz, *Member, IEEE*, and Steven B. Leeb, *Fellow, IEEE*

***Abstract*—This paper presents a retrofit system that exploits a fluorescent lamp's own stray electric fields for capacitive sensing. Occupancy detection for demand-side energy management is a key application. The experimental system demonstrates a detection range of 10 ft. between the lamp and the nearest edge of the occupant. A full system model is presented including the simulation of a lumped element capacitive model. The full system model is validated against experimental data.**

***Index Terms*—Capacitive model, capacitive sensing, FastCap, fluorescent lamp, fully-differential, occupancy sensing, SPICE.**

I. INTRODUCTION

The U.S. Department of Energy has identified "sensing and measurement" as one of the "five fundamental technologies" essential for driving the creation of a "Smart Grid" [1]. In 2008, occupant-oriented loads such as lighting, and heating, ventilation and air conditioning (HVAC) accounted for roughly 20% and 33% of the total delivered electricity, respectively [2]. The integration of smart grid-enabled control into industrial power electronic systems and occupant-based control of lighting have been shown to provide substantial benefits in this regard [3]–[5].

This paper presents an occupancy detector that exploits a fluorescent lamp's own stray electric fields as an excitation source for capacitive sensing (the lamp sensor). Reuse of in-place fluorescent lamp infrastructure should support low-cost, widespread deployment. Additionally, the sensor measures electric fields rather than IR, so the usual limitations associated with PIR sensors are eliminated and true presence detection is feasible. Finally, by incorporating the sensor electronics in fluorescent lamps, control of lighting based on occupancy detection can be particularly straightforward. Reference [6] details an application example in which the lamp sensor directly controls the lamp's power consumption using a custom dimming fluorescent lamp ballast [7]–[11]. Significantly, [6] demonstrates good detection sensitivity even at very low bulb power (1%). The "autodimming" lamp obviates the need for frequent lamp ignition which has been shown to impact bulb life [9], [12].

Pyroelectric Infrared (PIR) sensors have been used extensively for low-cost occupancy detection [13]–[15]. Typically, the ability of a PIR sensor to function as a presence detector is limited by low-frequency noise or drift from changes in background infrared radiation (IR). The measured signals can be bandlimited (high-pass filtered), but the sensor effectively becomes a motion sensor, not a presence sensor [13], [14]. As an alternative to PIR sensors, [16] presents a retrofit capacitive sensor for detecting occupants using in-place utility wiring and demonstrates detection ranges of about 1 m from the wire to the occupant. The sensor presented here demonstrates detection ranges approximately three times as long as those in [16].

The main contribution of this work over the previous work in [6], [17]–[20] is a full system model validated against experimental data. It includes a lumped element capacitive model of the sensor system coupled with a circuit model of the fully-differential current-mode front end amplifier developed in Section III. The modeling concepts in Section II have been developed significantly beyond previous work to advance our understanding of the system operating principles and to develop an accurate full system model. Furthermore, the analysis and evaluation of the signal conditioning electronics in Section III has been expanded with respect to the design process and noise performance.

Section II reviews and develops the basic operating principles and modeling of the lamp sensor system. Section III presents the implementation of a lamp sensor including a discussion of key design principles and experimental data from a cart-mounted lamp sensor. Section IV presents a new full system model and validates it against experimental data from a hanging lamp sensor.

II. OPERATION AND MODELING

The operation of the lampsensor system can be understood with a capacitive abstraction which models the behavior of the electrostatic fields coupling the conducting objects below the lamp. Implicit in this abstraction is the assumption that the electric fields vary slowly enough that the system is quasistatic—an assumption that holds for any reasonable lamp ballast operating frequency (10–100 kHz). In this section, the link between electrostatic field modeling and the capacitive abstraction is briefly reviewed starting from Maxwell's equations. Then, the development of a capacitive model is discussed by considering models of the key system elements.

Manuscript received September 13, 2010; revised December 20, 2010 and March 8, 2011; accepted April 13, 2011. Date of publication May 5, 2011; date of current version November 1, 2011. This work was supported by the Grainger foundation, the MIT Energy Initiative, the U.S. Department of Energy, and the Grainger Foundation.

The authors are with the Massachusetts Institute of Technology, Cambridge, MA 02139 USA (e-mail: jjcooley@mit.edu; avestruz@mit.edu; sbleeb@mit.edu).

Color versions of one or more of the figures in this paper are available online at http://ieeexplore.ieee.org.

Digital Object Identifier 10.1109/TIE.2011.2151816

The boundary conditions that arise from Faraday's law and Ampere's law in Maxwell's equations are

$$\hat{n} \times (\vec{E}_1 - \vec{E}_2) = 0 \tag{1}$$

$$\hat{n} \cdot (\vec{E}_1 - \vec{E}_2) = \frac{\rho_s}{\epsilon}. \tag{2}$$

Equations (1) and (2) imply that the electric field at a conducting boundary terminates normal to the conducting surface with a magnitude of ρ_s/ϵ. The resulting charge in an area, A, on the surface of a conductor is

$$\begin{aligned} Q(t) &= \iint\limits_A \rho_s(t)\, dA \\ &= \epsilon \iint\limits_A \vec{E}_n(t) \cdot d\vec{A} \\ &= \epsilon \Phi_e(t) \end{aligned} \tag{3}$$

where $\Phi_e(t)$ is the total electric flux impinging normal to the surface with area A. If the electric field impinging on the surface of the conductor is the result of the potential on a second conductor, dividing the total charge on either conductor by their potential difference yields the capacitance

$$C \equiv \frac{\epsilon \int\int_A \vec{E}_n(t) \cdot d\vec{A}}{\int_s \vec{E}(t) \cdot d\vec{s}} = \epsilon \frac{\Phi_e(t)}{v_c(t)}. \tag{4}$$

The current drawn onto a surface of area, A, is the time derivative of the total charge in that area

$$I(t) = \frac{\partial Q(t)}{\partial t} = \epsilon \frac{\partial \Phi_e(t)}{\partial t} \tag{5}$$

and combining (4) with (5) reveals the familiar result

$$I(t) = C \frac{\partial v_c(t)}{\partial t}. \tag{6}$$

Equation (5) explicitly describes the relationship between capacitively coupled current and the time-derivative of the impressed electric field.

The capacitive abstraction approach in this work generally attempts to lump conducting objects in the lamp sensor system as nodes in a circuit model. For instance, the backplane of the lamp, the measurement electrodes, and other large unmovable conducting objects in the detection field are taken as conducting nodes in the system. References [16] and [21]–[23] set precedents for treating a human as a conducting shell (Fig. 1). Therefore, the human occupant is also taken as a conducting (and moving) node in the system.

A. Modeling the Floor

It is difficult to generalize the floor below the lamp as a conducting or a nonconducting plane. The correct treatment is perhaps dependent on the particular construction of any given floor. Moreover, if the floor is taken as a conducting plane, it must be determined if it is sufficiently well-connected to any reference potentials in the system, e.g., earth ground. Section IV describes a method for controlling these ambiguities by iteratively comparing simulated results to experimental data.

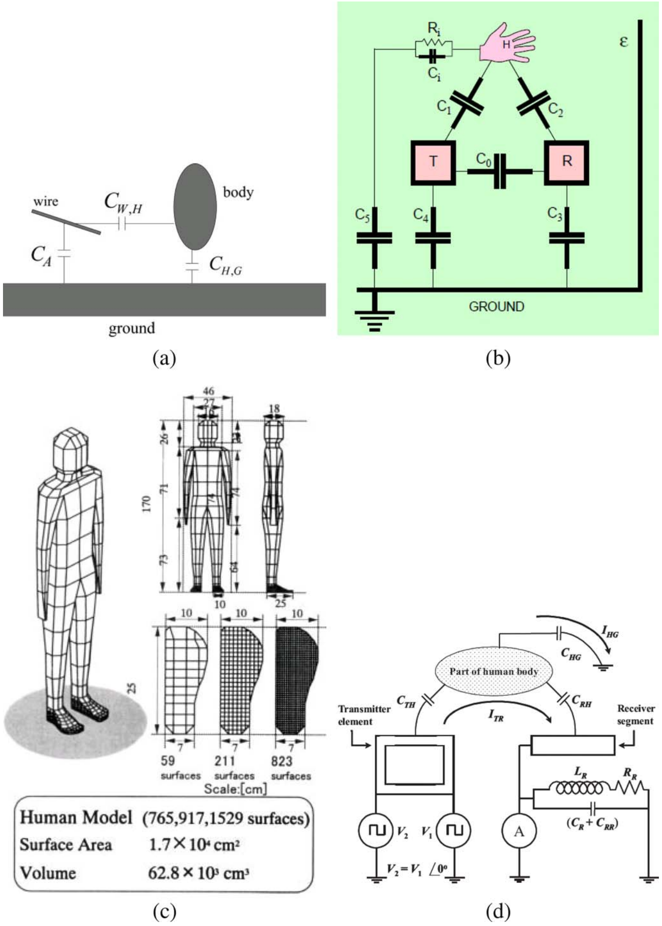

Fig. 1. Examples of systems with human conductor models taken from [16] and [21]–[23].

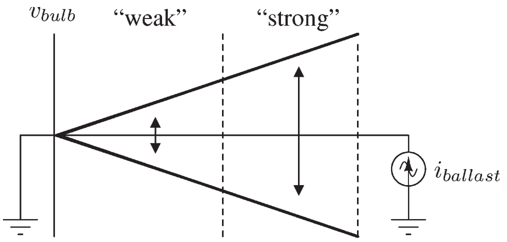

Fig. 2. Alternating linear voltage profile of a resistive bulb.

B. Modeling the Source

The signal source in the lamp sensor is derived from stray electric fields that couple from the ends and surfaces of the bulbs to the other conducting objects in the system. Lumping a single bulb into two pieces and comparing the resulting source impedance to the capacitive impedances that load it reveals that a voltage source (as opposed to a current source) representation is reasonable [9], [17], [24]. Having chosen a voltage source representation, the two pieces of the lumped signal source model may be assigned corresponding (alternating) potentials.

Fig. 2 depicts the alternating linear voltage profile along the length of a driven resistive bulb. If the bulb is lumped into

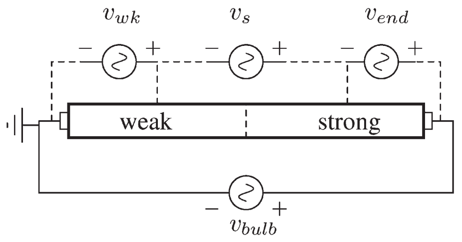

Fig. 3. Two bulb halves comprise the lumped element model of a single bulb.

two halves, the half closer to the driven end may be called the "strong" half because the potentials in that piece vary a lot with respect to the undriven end (the ballast common). Then, the half closer to the undriven end may be called the "weak" half for obvious reasons. A corresponding lumped element model of a single driven fluorescent bulb is depicted in Fig. 3. In Section IV, a capacitive model is evaluated in which the signal source derived from a two-bulb lamp is represented using two lumped-element models like the one shown in Fig. 3.

C. Signal Source Reference

In this electrostatic system, it is important to establish conceptions of the reference potentials and surfaces that support current return paths as we develop lumped-element models of the system. Because the signal source itself is a conceived electrostatic model of a driven fluorescent bulbs, the signal source reference potential and its physical location in the system is perhaps ambiguous. A convenient choice for the signal source reference is the ballast common shown as a ground symbol in Fig. 3 because a) it is separated from the weak node in the bulb model by a relatively small (alternating) potential difference and b) it is a physical node in a the ballast circuit that allows for explicit ohmic connections. Therefore, in this work, the ballast common is called the "signal source reference" and those two node names are used interchangeably.

D. Capacitive Models and Limitations

Having lumped all of the key elements in the system as conducting, and possibly driven nodes, the electric field behavior may be captured by considering the capacitive coupling between those nodes. Proceeding along these lines, a circuit model of the relatively complicated system can be drawn. The signal conditioning electronics can be taken to connect to that circuit at the electrode nodes and the system response can be determined by various means. An example of such a full system model is presented and evaluated in Section IV using capacitance extraction software and a SPICE simulation.

Perhaps the primary limitation of the lumped element capacitive model originates in the modeling of the signal source. The electric field is related to the spatial derivative (gradient) of the corresponding scalar potential field, i.e., $\vec{E} = -\nabla\varphi$. When the bulb is lumped into two distinct halves and each half assigned a single potential, the variation of the actual potential along the length of those sections is neglected. Furthermore, abrupt changes are implicitly introduced in the potential at the ends of the bulb halves. The electric field corresponding to the lumped element model is inevitably an approximation of the actual electric field. Nonetheless, Section IV will show that the approximations inherent to the lumped-element model allow for acceptable prediction of the system behavior.

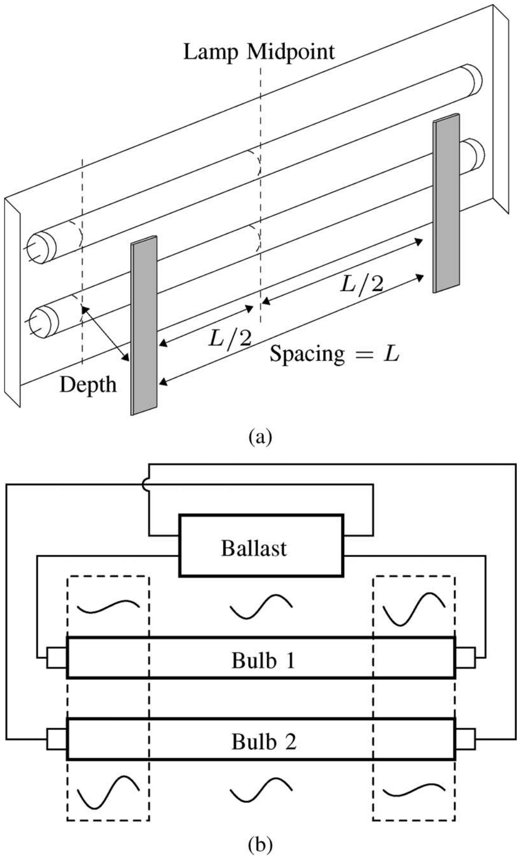

Fig. 4. Lamp configuration for a symmetrical signal source leading to natural carrier suppression. (a) Physical configuration and (b) electrical configuration.

III. IMPLEMENTATION

A lamp sensor was implemented to evaluate its feasibility as an occupancy detector. The configuration of the experimental two-bulb lamp is depicted in Fig. 4. The physical configuration shown in Fig. 4(a) includes two measurement electrodes spaced symmetrically about the center of the lamp. The electrical configuration shown in Fig. 4(b) reverses the ballast connections to one of the two bulbs. The result is a symmetrical electric field source. Coupling this lamp and electrode configuration with a differential measurement yields a natural suppression of unneeded carrier content. This carrier suppression is important for detecting very small perturbations of the capacitive system caused by the occupant below the lamp.

A fully-differential transimpedance amplifier [Fig. 5(a)] was chosen for the front-end amplifier. Current-mode detection was needed to accurately measure signals in the high impedance capacitive network. An analytical modeling effort was undertaken to accurately describe the operation of the fully-differential amplifier. The resulting circuit model in Fig. 5(b) represents both the differential-mode and common-mode current paths through the amplifier.

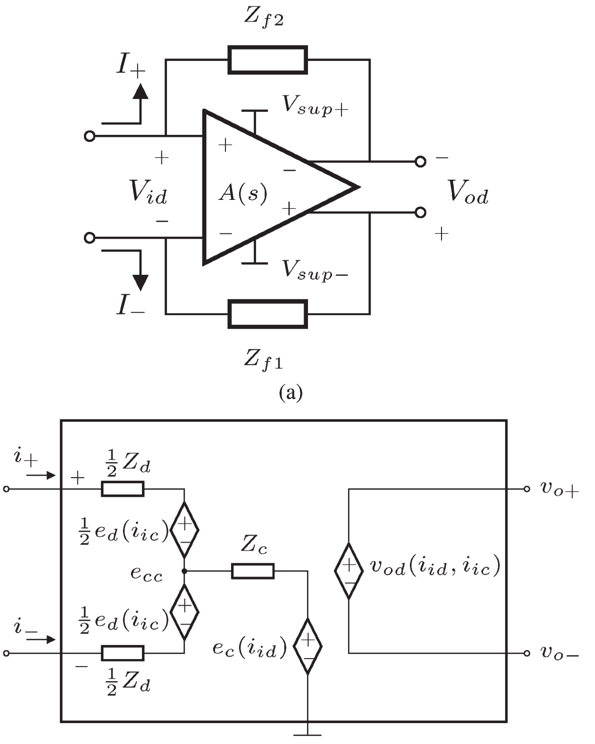

(a)

(b)

Fig. 5. Fully-differential transimpedance amplifier and a small-signal model. (a) A fully-differential transimpedance amplifier. (b) A small-signal T-model.

The model parameters can be derived through analysis. Using a linear superposition approach, the differential- mode output voltage is

$$v_{od} = \left(\frac{2\overline{Z_f}a_d - \frac{1}{2}a_c\Delta Z_f}{(1+a_d)}\right)i_{id} + \left(\frac{a_c\overline{Z_f} - a_d\Delta Z_f}{2(1+a_d)}\right)i_{ic} \tag{7}$$

where i_{id} is the differential-mode (DM) input current, i_{ic} is the common-mode (CM) input current, a_d is the op-amp DM-DM gain, a_c is the op-amp CM-DM gain and

$$\overline{Z_f} \equiv \frac{(Z_{f1} + Z_{f2})}{2} \tag{8}$$

$$\Delta Z_f \equiv Z_{f1} - Z_{f2}. \tag{9}$$

Examining the differential-mode output voltage in (7), the term multiplying i_{id} is the differential-mode transimpedance and describes the dominant behavior of the amplifier. For the perfectly ideal case, $a_d \to \infty$, $a_c \to 0$, and $\Delta Z_f \to 0\ \Omega$, the "fully-ideal" output voltage becomes

$$\boxed{v_{od} = 2\overline{Z_f}i_{id}}\,. \tag{10}$$

A similar analysis leads to expressions for the common-mode and differential-mode input voltages

$$v_{ic} = -i_{id}\frac{\Delta Z_f}{2} + i_{ic}\frac{\overline{Z_f}}{2} \tag{11}$$

$$v_{id} = i_{id}\left(\frac{2\overline{Z_f} + \frac{1}{2}\Delta Z_f a_c}{(1+a_d)}\right) - i_{ic}\left(\frac{\Delta Z_f + \overline{Z_f}a_c}{2(1+a_d)}\right). \tag{12}$$

TABLE I
TYPICAL SYSTEM PARAMETERS AND PASSIVE COMPONENTS

Parameter	Value
$R_{f1,2}$	10 MΩ
$C_{f1,2}$	7.5 pF
R_{f3}	200 kΩ
C_{f3}	660 pF
R_{lim}	20 Ω
R_{pu}	500 Ω
R_{lpf}	10 kΩ
C_{lpf}	150 pF
f_{carr}	50 kHz

Based on the analytical results in (7)–(12), the approximate circuit model parameters are

$$Z_c = \left(\frac{\overline{Z_f}}{2}\right) \tag{13}$$

$$Z_d = \left(\frac{2\overline{Z_f} + \frac{1}{2}\Delta Z_f a_c}{(1+a_d)}\right) \tag{14}$$

$$e_c(i_{id}) = -i_{id}\left(\frac{\Delta Z_f}{2}\right) \tag{15}$$

$$e_d(i_{ic}) = i_{ic}\left(-\frac{\Delta Z_f}{2(1+a_d)} - \frac{\overline{Z_f}a_c}{2(1+a_d)}\right). \tag{16}$$

Notably, the model indicates a low impedance path for purely differential-mode input currents, i.e., a differential- mode virtual short-circuit between the input nodes of the amplifier. Accordingly, the fully-differential transimpedance amplifier may be approximated as a short circuit between the measurement electrodes. Its output voltage is proportional to the current that flows through that short circuit according to (10). The circuit model in Fig. 5(b) is validated as part of the full system model in Section IV.

The front end amplifier was implemented with a fully-differential op-amp in a closed-loop transimpedance configuration. The feedback components for the front end were chosen to satisfy constraints in noise performance and closed-loop stability. The AD8620 op-amps shown in Fig. 8 were chosen for their JFET input devices, which draw very little input bias current and input-referred current noise. A schematic of the signal conditioning circuit is shown in Fig. 8. Typical system parameters and passive component values are shown in Table I.

A. Synchronous Detection

The block diagram in Fig. 6 illustrates the synchronous detection scheme. The carrier signal is the high- frequency alternating signal source originating in the fluorescent lamp. Presence of the occupant in the detection field changes the amount of capacitive coupling from the lamp to the electrodes and thus the amount of current input to the front end. This modulation effect is represented in Fig. 6 with a variable capacitor, C_{meas}. A copy of the (unmodulated) carrier signal is fed forward and multiplied with the output of the front end amplifier. Multiplication by this phase reference achieves specificity in phase and frequency leading to a significant rejection of unwanted signals. A low-pass filter (LPF) attenuates the high-frequency residue after demodulation to yield the low-frequency modulations caused by the occupant below the

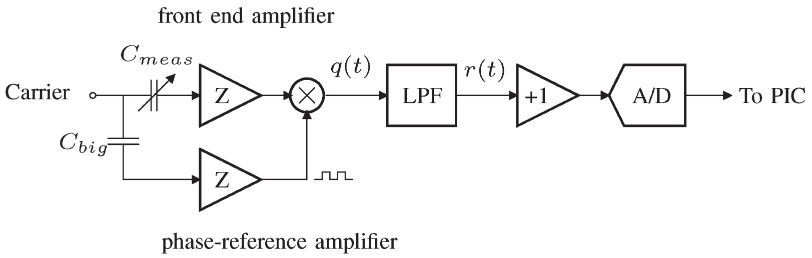

Fig. 6. Block diagram of the signal conditioning system. Transimpedance amplifiers are marked with a “Z”.

lamp. From [25], the output of such a synchronous detector, can be approximated as

$$\boxed{r(t) = \tfrac{4}{\pi}\overline{Z_f} I_{id}(t)\cos\phi} \tag{17}$$

in which $I_{id}(t)$ is the amplitude of the differential-mode input current to the front end, $\overline{Z_f}$ is the nominal front end feedback impedance value and ϕ is the phase error between the front end output and the phase reference.

The fully-differential multiplier was implemented with a full bridge of analog switches controlled according to the measured phase reference signal. Two chopper-stabilized op-amps buffered the output of the LPF decoupling the frequency response design constraints of the LPF from the maximum source impedance constraints specified for the A/D [26]. Because band-limiting effects in the final A/D are significant, the LPF may be viewed as an anti-aliasing filter while the majority of interpolation occurs in the A/D itself. A typical sampling rate for the A/D is 14 sps. Taking the corresponding Nyquist rate (7 Hz) as the low-pass bandwidth, the synchronous detector will largely reject unwanted signals whose frequency differs from that of the desired signal by more than 7 Hz. Given typical carrier frequencies near 50 kHz, the synchronous detector effectively achieves extremely aggressive bandlimiting of the incoming modulated signal.

1) Phase Reference: The phase reference was measured with a single-ended transimpedance amplifier (Fig. 8) capacitively-coupled to the bulbs. The phase reference electrode can be taped to the bulb or to a driven ballast wire. It can also be built into the ballast as a trace adjacent to the drive signal for the bulb or as an explicit capacitor coupling to the ballast drive signal.

The feedback components for the single-ended phase reference amplifier were chosen to match its phase contribution to that of the front end amplifier. With the passive component values from Table I, the magnitude and phase of the phase-reference transimpedance were

$$|Z_{f3}| = 4.82\ \Omega \tag{18}$$

$$\angle Z_{f3} = -88.6^\circ \tag{19}$$

and for the front end amplifier, they were

$$|2\overline{Z_f}| = 424\ \mathrm{k}\Omega \tag{20}$$

$$\angle 2\overline{Z_f} = -87.6^\circ \tag{21}$$

leading to a phase error of $\phi = 1^\circ$ between the front end and phase-reference amplifiers and a corresponding multiplicative error factor from (17) of

$$\eta = \cos 1^\circ \approx 0.99985. \tag{22}$$

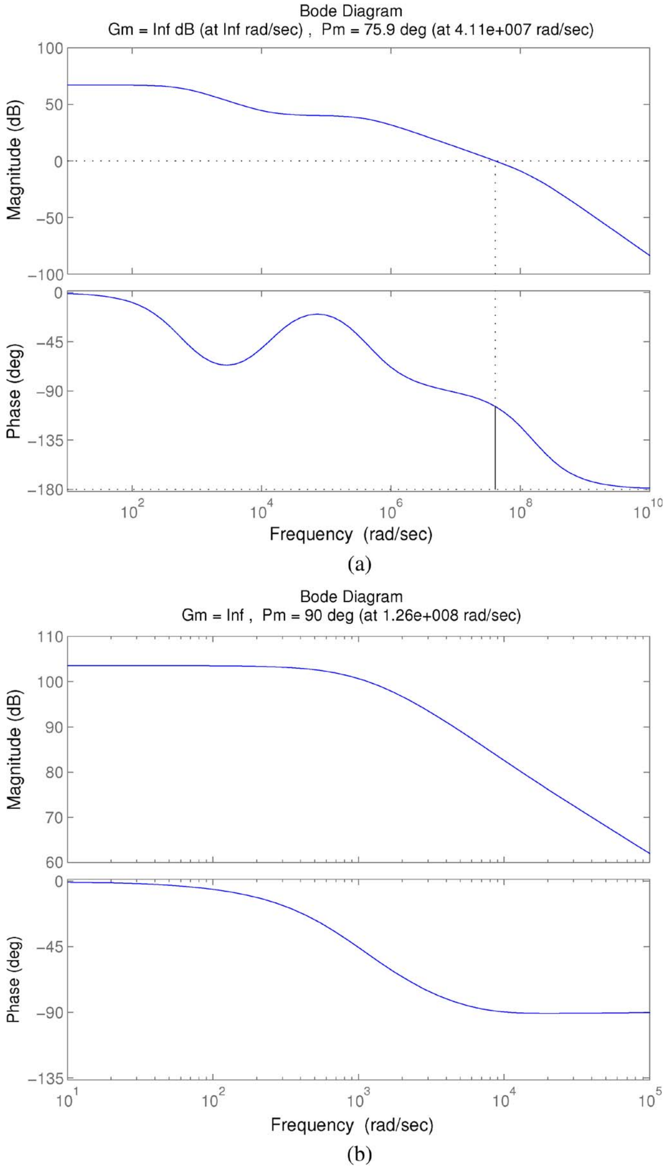

Fig. 7. Open-loop frequency responses showing suitable phase margin. (a) Front end, P.M. $= 75.9^\circ$ and (b) phase-reference, P.M. $= 90^\circ$.

B. Stability

Analysis of the front end amplifier shown in Fig. 8 leads to the following loop-transfer function:

$$\boxed{L(s) = a_d(s)H_J(s)\frac{Z}{Z+Z_f}} \tag{23}$$

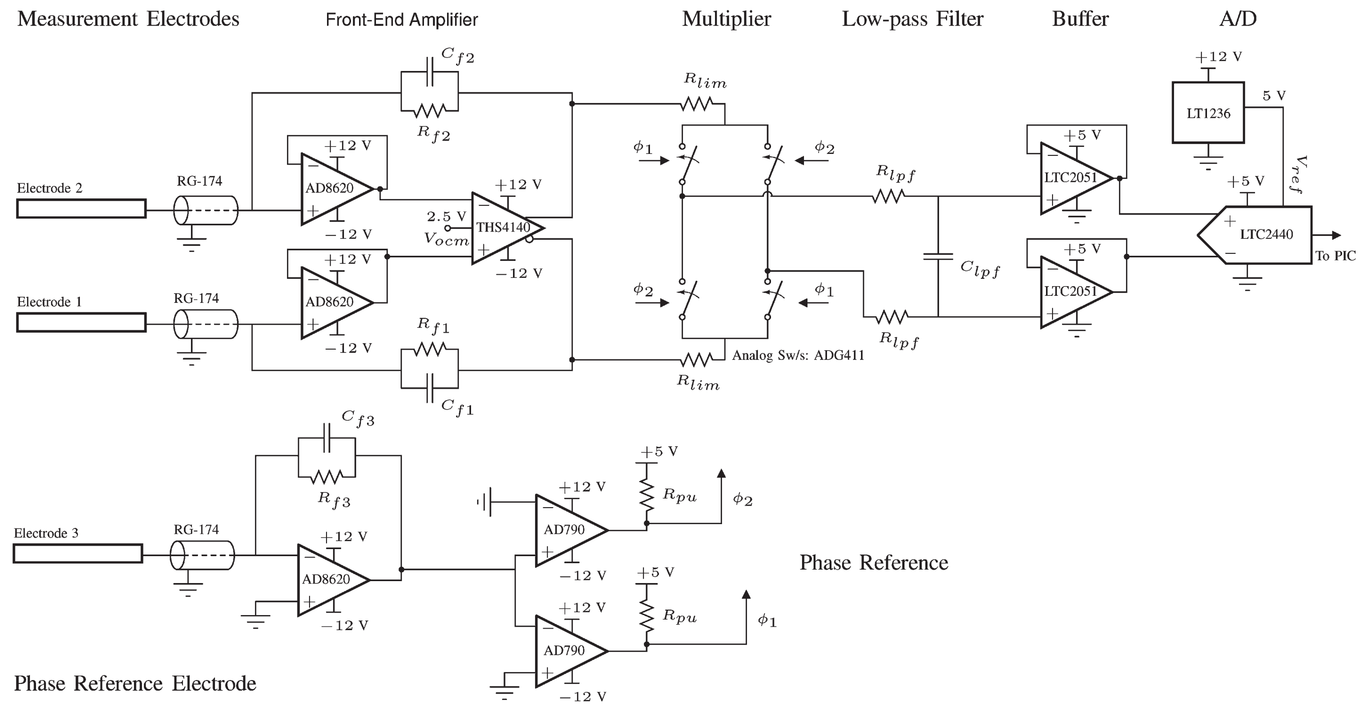

Fig. 8. Simplified schematic of the fully differential signal conditioning electronics.

where $H_J(s)$ is the closed-loop transfer function of the buffer op-amps (AD8620), $a_d(s)$ is the differential-mode gain of the THS4140 fully-differential op-amp, Z is the nominal impedance between the op-amp inputs and incremental ground, and Z_f is the nominal feedback impedance. A similar analysis leads to the loop transfer function for the (single-ended) phase-reference amplifier

$$\boxed{L_p(s) = a_J(s)\frac{Z}{Z+Z_{f3}}} \tag{24}$$

in which $a_J(s)$ is the differential-mode voltage gain of the AD8620 op-amp, Z is the impedance between the op- amp inverting input and incremental ground and Z_{f3} is the value of the amplifier's feedback impedance. Stray input capacitances to incremental ground contribute to Z in (23) and (24). These include the coaxial shield capacitance from the electrode cables, stray capacitances between PCB traces and the input capacitance of the AD8620 op- amps in the front end amplifier. With the lamp sensor powered off, the feedback passive components, R_{f1} and C_{f1}, removed from the PCB and an electrode with a 36-in RG-174 electrode cable attached to the input node, the stray capacitance measured for one input was 159 pF.

Bode plots of the loop transfer functions with the passive components from Table I are shown in Fig. 7. Both plots show good phase margin indicating suitable stability. Closer examination of the loop-transfer functions reveals the manner in which the feedback compensation achieves closed-loop stability. The loop-transfer, $L(s)$, for the front end can be rewritten as

$$L(s) = a_d(s)H_J(s)\left(\frac{1+R_f sC_f}{1+R_f s(C_{in}+C_f)}\right) \tag{25}$$

where C_{in} is the total capacitance from the either input node to ground. With dominant pole models the op-amp dynamics, the gain terms, $a_d(s)$ and $H_J(s)$, each contribute one pole but no zeros. The addition of R_f contributes one additional pole and the addition of C_f contributes one additional zero (consider (25) for $C_f = 0$). The additional zero in the vicinity of at least one of the poles significantly reduces the phase lag of the loop transfer function near cross-over, thereby increasing the phase margin of the system. The incorporation of the parallel capacitance, C_f, in the feedback network is a form of lead compensation because it adds leading phase shift or positive phase to the output signal relative to the input signal at all frequencies [27].

C. Noise

The electronics were designed to contribute less noise to the final output than the noise inherent in the measured signal. To evaluate our efforts in this regard, the noise contributions from the implemented electronics were enumerated analytically. Because the noise inherent in the measured signal is most easily quantified empirically, experimental data ultimately verified the low-noise design. The total noise voltage contribution of the front end amplifier at the A/D input (the output of the synchronous detector) is (26), shown at the bottom of the next page, in which Z is comprised of stray input capacitances. The complex impedances may be taken as their values at the carrier frequency because the synchronous detector output is narrowband [25]. Also e_{nT} and e_{nJ} are the input-referred voltage noises for the THS4140 and AD8620 parts, respectively, i_{nJ} is the input-referred current noise of the AD8620 part, k is the Boltzmann constant, T is temperature, R_f is the nominal feedback resistance in the front end, and ω_c is the carrier or ballast operating frequency. Finally, BW_n is the noise

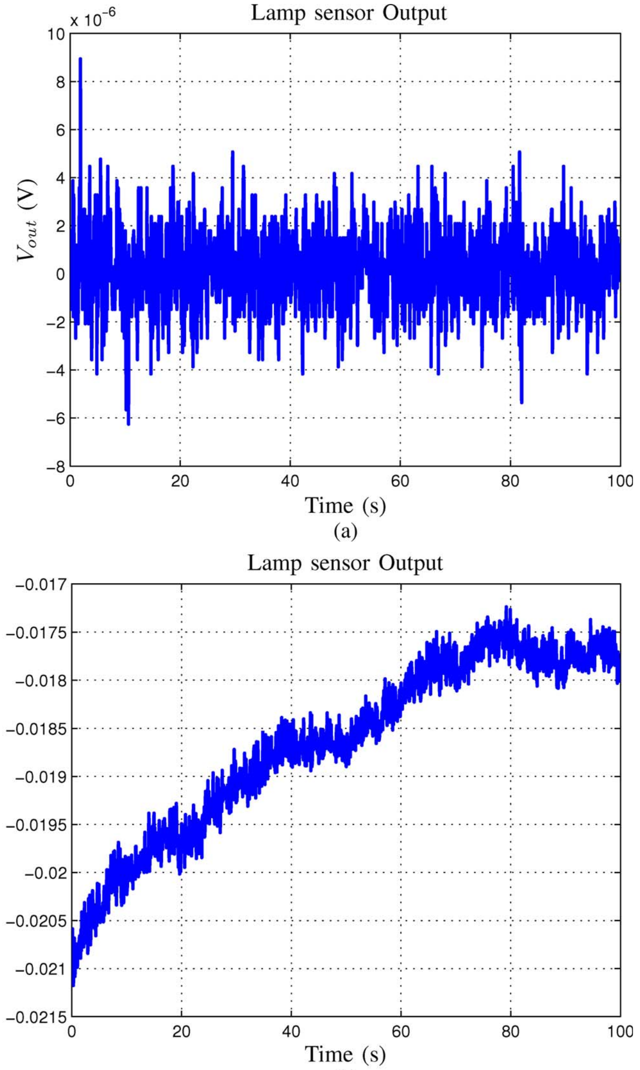

(a)

(b)

Fig. 9. Noise Data: values are average noise levels in a 10-s window. (a) Without Lamp: Peak deviation: 15 μV, Avg. ac rms noise in 10-s window: 2.51 $\mu\mathrm{V}_{\mathrm{rms}}$ and (b) with Lamp: Peak deviation: 3.9 mV, Avg. ac rms noise in 10-s window: 186 $\mu\mathrm{V}_{\mathrm{rms}}$.

bandwidth and is ultimately constrained by the A/D to be 12.4 Hz for a typical sampling rate of 14 sps. Using (26), the passive component values in Table I, and the datasheets for the parts in Fig. 8, the noise sources at the input to the A/D are

$$v_{n,\mathrm{amp}} = 500\ \mathrm{nV}_{\mathrm{rms}} \tag{27}$$

$$v_{n,\mathrm{buff}} = 1.5\ \mu\mathrm{V}_{p-p},\ \text{typical in } 0.1 - 10\ \mathrm{Hz} \tag{28}$$

$$v_{n,\mathrm{AD}} = 250\ \mathrm{nV}_{\mathrm{rms}}. \tag{29}$$

From (27)–(29), the dominant noise source originates in the buffers that precede the A/D inputs. Therefore, the front end is suitably low-noise in the sense that it is *not* the dominant noise source. Whether or not the electronics as a whole are suitably low-noise depends on the noise content inherent in the measured signals. Time-domain plots of typical noise at the lamp sensor output are shown in Fig. 9. Comparing the noise in

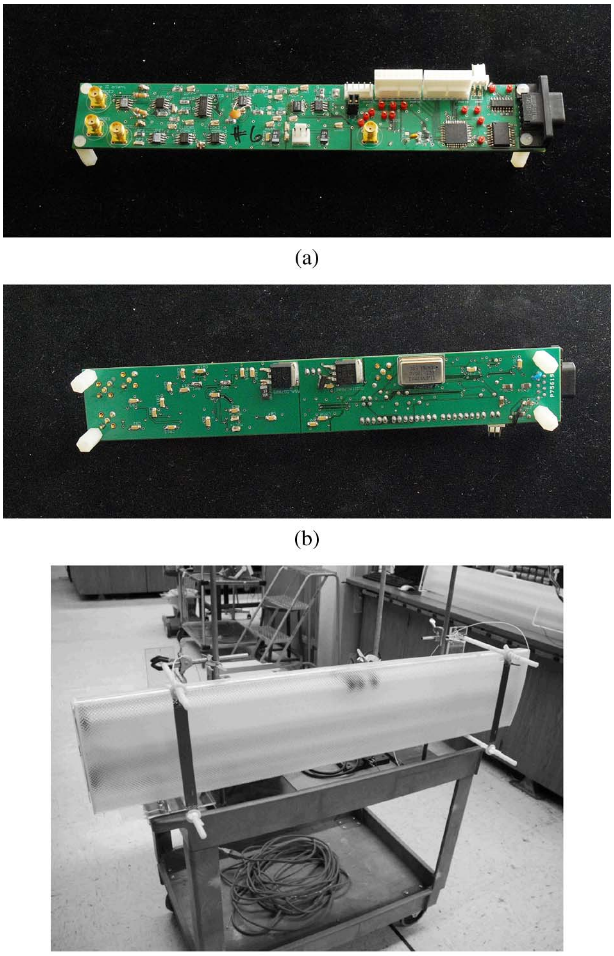

(a)

(b)

(c)

Fig. 10. Photographs of the cart mounted experimental setup and lamp sensor electronics. (a) Lamp sensor PCB: top; (b) lamp sensor PCB: bottom; and (c) the Cart-mounted lamp experimental setup.

TABLE II
RANGE TEST EXPERIMENTAL SETUP PARAMETERS

Parameter	Note / Value
$R_{f1,2}$	1 MΩ
$C_{f1,2}$	1 pF
R_{f3}	80 kΩ
C_{f3}	30 pF
f_{carr}	42 kHz
Phase Ref Elect.	Taped to bulb center
Earth, gnd, Common	Not explicitly connected
Ballast	Commercial ballast
Bulbs	2×T8 32 W @ full power

$$v_{n,\mathrm{amp}} \approx \frac{2}{\pi}\sqrt{BW}_n \sqrt{\left(\left(e_{nT}^2 + 2e_{nJ}^2\right) \left(\frac{Z_f}{Z}\right)^2_{\omega_c} + \left(2i_{nJ}^2 + 2\frac{4kT}{R_f}\right) Z_f|^2_{\omega_c} \right)}\, V_{\mathrm{rms}} \tag{26}$$

TABLE III
DETECTION DATA p—VALUES FOR VARIOUS ELECTRODE CONFIGURATIONS AT THE LIMIT OF THE DETECTION RANGE

Spacing (in.)	Depth (in.)	p-values 7ft.	8ft.	9ft.	10ft.	11ft.	Noise Floor ($\mu V_{ac,rms}$)
44	5	0	0	0	2.53×10^{-4}	0.328	54.5
	4	0	0	4.63×10^{-7}	0.0165	N/A	65.1
	3	0	0	0	4.85×10^{-6}	0.661	98.9
	2	0	$< 10^{-7}$	0.0426	N/A	N/A	168.5
38	5	0	0	3.05×10^{-5}	0.0240	N/A	61.8
	4	0	0	4.93×10^{-5}	0.865	N/A	67.3
	3	0	0	$< 10^{-7}$	0.133	N/A	62.7
	2	0	0	0.00200	0.0160	N/A	74.0
28	5	0	0	0	$< 10^{-7}$	0.306	45.2
	4	0	0	1.19×10^{-4}	0.676	N/A	70.7
	3	0	0	$< 10^{-7}$	0.884	N/A	52.3
	2	0	2.62×10^{-5}	0.00100	0.0270	N/A	65.3
19	5	0	$< 10^{-7}$	0.382	N/A	N/A	55.4
	4	0	0	$< 10^{-7}$	0.126	N/A	41.6
	3	0	$< 10^{-7}$	0.0120	N/A	N/A	45.4
	2	0	0	1.01×10^{-5}	0.0340	N/A	42.2
15	5	0	$< 10^{-7}$	0.0360	N/A	N/A	40.9
	4	$< 10^{-7}$	0.0210	N/A	N/A	N/A	51.5
	3	0	$< 10^{-7}$	0.0640	N/A	N/A	49.9
	2	$< 10^{-7}$	0.0120	N/A	N/A	N/A	57.2

Fig. 9(a) to that in Fig. 9(b) reveals that the signal conditioning electronics contribute negligibly to the overall noise content. Therefore, the signal conditioning electronics are suitably low-noise.

D. Range Test

To evaluate the sensitivity of the implemented lamp sensor, a range test was performed. A cart-mounted system, shown in Fig. 10(c), was constructed to collect sensitivity data. Fig. 10(a) and (b) show photographs of a lamp sensor PCB. Experimental setup parameters including passive component values for the sensor are shown in Table II.

Data was taken for 20 different electrode configurations. Each configuration consisted of an electrode spacing and depth as defined in Fig. 4(a). Each sample consisted of one pass of a human occupant walking in front of the horizontally mounted lamp. The metric for each sample was the ac rms output voltage, $V_{ac,\mathrm{rms}}$. For each configuration, 10 control samples (noise floor measurements) were taken with no occupant. Then, for each range in each electrode configuration, 5 samples were taken with a occupant passing in front of the lamp. A Z-test in MATLAB was performed on the data comparing each 5-sample data set for each range to the control data set for the corresponding electrode configuration. In our detection rule, the sample data sets had to demonstrate a mean $V_{ac,\mathrm{rms}}$ larger than that of the control data sets with a confidence level of 99% or better. The resulting statistical data are shown in Table III at the boundary of the detection range. The range varies along the columns. The electrode configuration varies along the rows. The data in Table III indicate detection ranges of 7–10 ft., depending on the electrode configuration (Fig. 11).

IV. FULL SYSTEM MODEL

This section presents and evaluates a full system model of the lamp sensor system. The model is a SPICE simulation of a

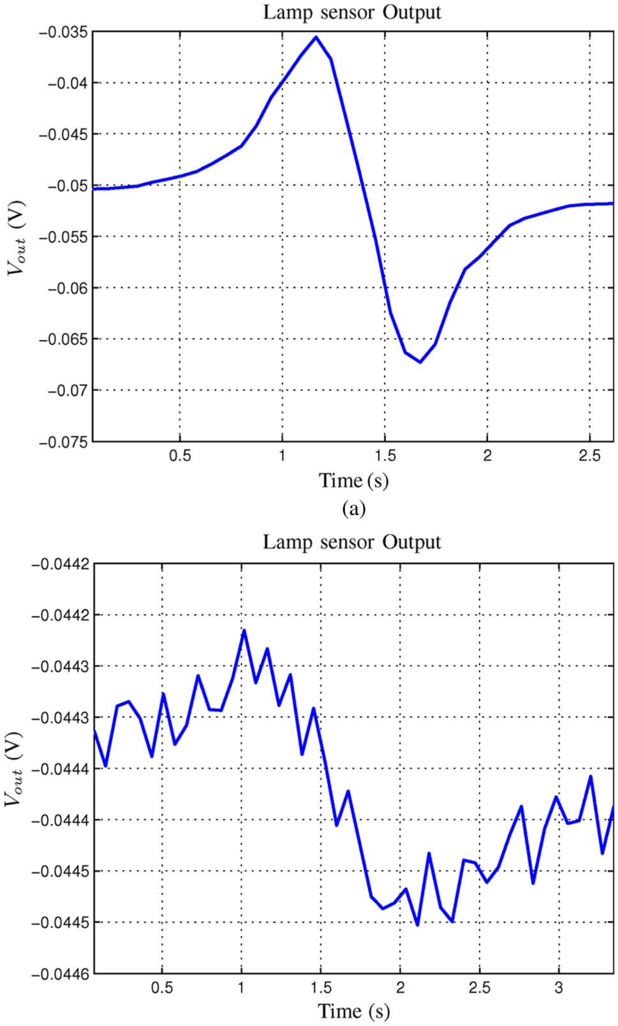

(a)

(b)

Fig. 11. Example output data plots taken from the range test for a passing occupant. (Configuration 44 × 5). (a) 4 ft. (b) 10 ft.

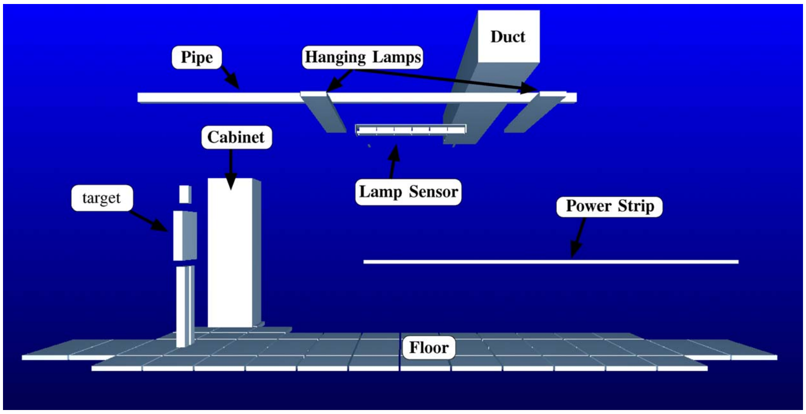

Fig. 12. Screenshot of the FastCap 3-D model.

TABLE IV
TYPICAL SIMULATED CAPACITANCES [SHOWN FOR A OCCUPANT POSITIONED UNDER THE LEFT END OF THE LAMP SENSOR DEPICTED IN FIGS. 12 AND 14(a)]

Capacitance	Value	Notes
		Vary with occupant
L. strong-occupant	300 fF	
R. strong-occupant	167 fF	
L. Electrode-occupant	534 fF	
R. Electrode-occupant	187 fF	
Backplane-occupant	14.3 pF	
Cabinet-occupant	2.5 pF	
		Assumed Fixed
L. strong-L. Electrode	477 fF	
L. strong-L. weak	126 fF	
L. strong-R. strong	41 fF	
L. strong-Cabinet	56 fF	
R. strong-Cabinet	62 fF	
L. weak-Cabinet	81 fF	
R. weak-Cabinet	53 fF	
L. Electrode-Cabinet	102 fF	
R. Electrode-Cabinet	52 fF	
Backplane-Cabinet	19 pF	
L. strong-R. Electrode	27 fF	
L. strong-Backplane	3 pF	
L. Electrode-Backplane	3.1 pF	
L. strong-R. weak	1.6 pF	
Floor-Backplane	79.7 pF	
Floor-Cabinet	121 pF	
Floor-L. strong	321 fF	
Floor-L. Electrode	401 fF	
Floor-occupant	42.4 pF	"Shoe Capacitance"

capacitive circuit model like the one described in Section II and the signal conditioning electronics from Section III. The circuit model from Fig. 5(b) is used to simulate the front end amplifier. A schematic of the full system model is shown in Fig. 16.

Capacitance extraction software—FastCap—was used to determine the lumped element capacitance values in the SPICE simulation [28]. Fig. 12 is a screenshot showing the 3-D model developed for this purpose. It includes the floor at the bottom, the human occupant on the left and the fluorescent lamp and electrodes (lamp sensor) above the center of the floor. Also included in the model are other unmovable conducting objects such as a large cabinet on the left, as well as overhead pipes, other lamps, a large duct and a power strip case that appears at waist level.

Typical simulated capacitances are shown in Table IV. Those capacitances represent the simulation of the occupant under the left edge of the lamp in Fig. 12 with the lamp at a height of 2.43 m. Several capacitances in simulation are taken to be fixed as the occupant moves under the lamp ("Assumed Fixed") while only a few are taken to vary while the occupant moves ("Vary with occupant"). When the occupant passes directly below the center of the lamp, many capacitances can also be assumed from symmetry.

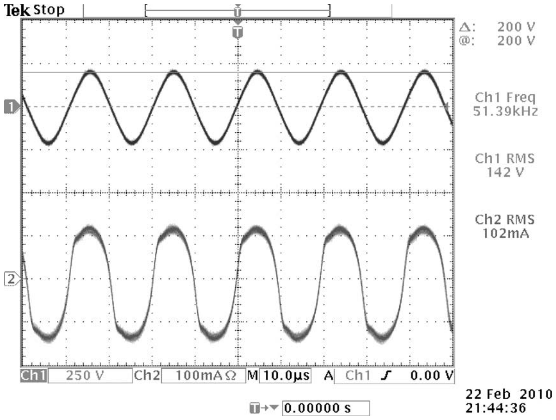

Fig. 13. Fluorescent bulb (top) voltage and (bottom) current: Custom dimming ballast 2 × T8 bulbs operated at 50% power.

A. Simulating the Floor

The floor in the experimental setup was a tile floor on top of a concrete slab of unknown construction. Two key questions arise: 1) Is the floor is well-represented by a conducting plane? and 2) If it is well-represented by a conducting plane, is it well-connected to reference potentials in the system, e.g., earth ground? To control these ambiguities, data from simulation was compared to data from the experimental system with and without an artificial conducting floor made of Aluminum foil. The artificial conducting floor was also connected and disconnected to or from the earth ground reference. Because little change was observed in the measured output from the experimental system among the three cases, it was speculated that the actual floor below the lamp was well-represented by an earthed conducting plane. In the SPICE model of Fig. 16, this was implemented as a short circuit between the "earth" and "floor" nodes. In the FastCap 3-D model of Fig. 12, this is manifested as a perfectly

TABLE V
SIMULATION PARAMETERS

Simulation Parameter	Note / Value	Source
$v_{bulb1,2}$	200 V	Oscilloscope (Figure 13)
$v_{s1,2}$	100 V	Model (Section II)
$v_{wk1,2}$	50 V	Model (Section II)
f_c	50 kHz	Oscilloscope (Figure 13)
$Z_{f1,2}$	423 kΩ	Calculated as $\|Z_f\|$ @ $\omega = 2\pi f_c$
Earth, gnd, Common	Explicitly connected	N/A
Electrode Depth	14.5 cm	Measured between electrodes and bulb surface
Electrode Spacing	98 cm	Measured between electrodes
Lamp Height	2.28, 2.43, 2.58 m	Measured between bulb surface and floor
occupant Height	1.83 m	Measured height of occupant
Effective Conducting Floor Depth	-2.5 cm	Empirical (Section IV-A)

conducting plane below the lamp and the occupant.[1] To account for the finite conductivity of the floor in our experimental setup the vertical position of the perfectly conducting plane in simulation ("effective conducting floor depth") was calibrated by comparing simulated and experimental data. The result, -2.5 cm, was determined empirically, by closely matching the peak deviation of simulated data taken from the SPICE simulation to the peak deviation of corresponding experimental data. The effective conducting floor depth was set using data with the lamp set at a height of 2.43 m and then held fixed for the other experiments.

B. Simulating the Source

Assuming a linear bulb voltage profile as in Fig. 2 we assign the model parameters for the signal source model in Fig. 3 as follows:

$$v_{wk} = \frac{1}{4} v_{\text{bulb}} \quad v_s = \frac{1}{2} v_{\text{bulb}} \quad v_{\text{end}} = \frac{1}{4} v_{\text{bulb}}. \tag{30}$$

Fig. 13 shows an oscilloscope shot of the bulb voltage and current under the experimental conditions. It shows a bulb voltage amplitude of 200 V and an operating frequency of about 50 kHz. With $v_{\text{bulb}} = 200$ V, the pieces of the signal source model become

$$v_{wk} = 50 \text{ V} \tag{31}$$

$$v_s = 100 \text{ V} \tag{32}$$

$$v_{end} = 50 \text{ V}. \tag{33}$$

The signal source model parameters are summarized in Table V. Note that the polarity and lack of phase shift between the measured bulb voltage and current validates the assumption that the bulb is well-modeled at high- frequency as a resistor consistent with [24]. The bulb voltage and current in Fig. 13 indicate a bulb resistance of approximately 1 kΩ.

C. "Earth," "GND," and "Common"

In the lamp sensor system, there are several "reference potentials" including the lamp sensor power supply ground ("gnd"), the ballast common ("common"), and earth ground ("earth"). To simplify the simulation, all of those reference potentials were explicitly shorted together in both the experimental setup and in simulation (see the bottom left of Fig. 16).[2] An ohm meter revealed that the pipes, fluorescent lamp backplanes, duct and power strip case were well connected to earth ground.

D. Simulation Procedure

The simulation was conducted using the FastCap model in Fig. 12. The extracted capacitances were inserted into the SPICE model shown in Fig. 16 and the simulated lamp sensor output voltage was read directly from SPICE.

Thirty seven separate simulations like the one depicted in Fig. 12 were used to model a passing occupant. For each simulation, the occupant was moved, in 20 cm increments, along the path that the real occupant in the experimental setup would take. The fixed capacitances listed as "assumed fixed" in Table IV were taken from a FastCap simulation with the occupant below the left end of the lamp. The simulated offset was measured by removing the occupant from the simulation. Simulation parameters are summarized in Table V.

---

[1] Segmenting the floor plane into smaller panels, as shown in Fig. 12, aided the FastCap simulator. In general, this method of breaking the conductors into pieces aided the simulation and was a practical necessity for getting the simulator to work properly. Common results yielded by a model without enough of this kind of granularity included "non-negative off-diagonals" and "failure to converge" errors as well as prohibitively long computation times.

[2] Shorting the ballast common to earth required that the L/N utility feed to the ballast be isolated.

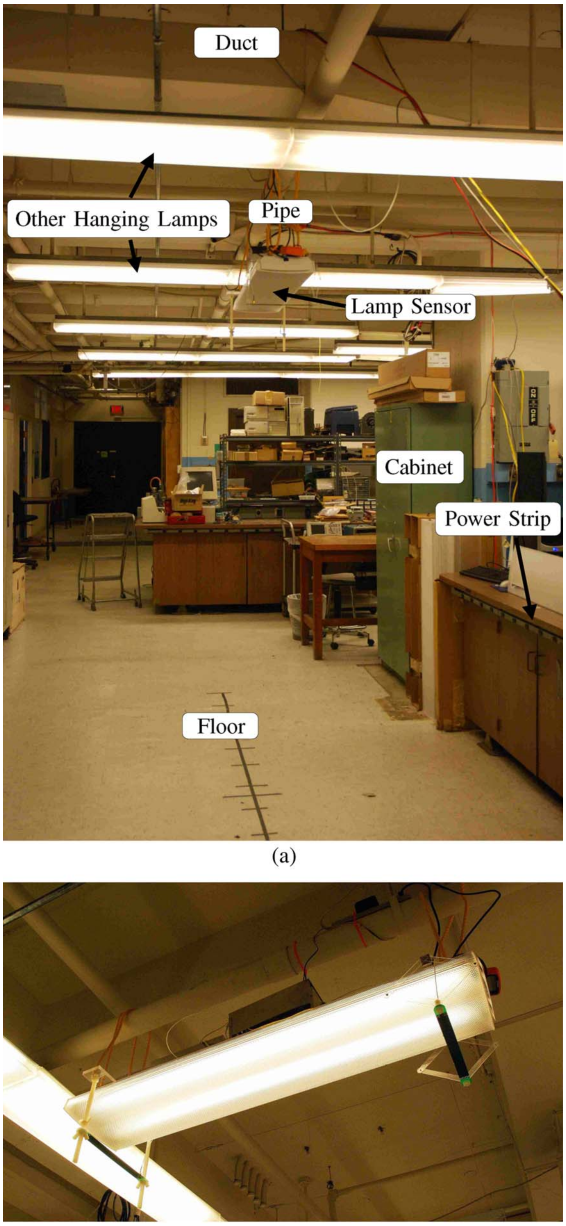

(a)

(b)

Fig. 14. Photographs of the hanging lamp experimental setup. (a) A photograph of the experimental setup. (b) A close-up photograph of the hanging lamp sensor.

E. Experimental Procedure

Experimental data was taken from the experimental setup shown in Fig. 14(a). Fig. 14(b), shows a close-up of the hanging lamp sensor and its adjustable electrodes.

Data was taken for the occupant passing through a detection field 7.2 m long positioned symmetrically about the center of the lamp [along the black line on the floor in Fig. 14(a)]. This path was chosen to correspond to the simulated path described in Section IV-D.

Thirty seven data points were taken from each pass in the experimental setup to ease the comparison to the simulated data. The experimental offset was measured as the value of the first data point taken from the sensor (corresponding to the case when the occupant is not well within the detection field). That offset was subtracted from all of the experimental data. Experimental setup parameters including passive component values for the sensor are summarized in Table VI.

TABLE VI
EXPERIMENTAL SETUP PARAMETERS

Experimental Parameter	Note / Value
$R_{f1,2}$	10 MΩ
$C_{f1,2}$	7.5 pF
R_{f3}	200 kΩ
C_{f3}	660 pF
f_c	50 kHz
Phase Ref Elect.	Integrated as Trace in Ballast
Earth, gnd, Common	Explicitly connected
Electrode Depth	14.5 cm
Electrode Spacing	98 cm
Lamp Height	2.28, 2.43, 2.58 m
occupant Height	1.83 m
Ballast	Custom Dimming Ballast see [6]
Bulbs	2xT8 32 W Operated at 50% Power

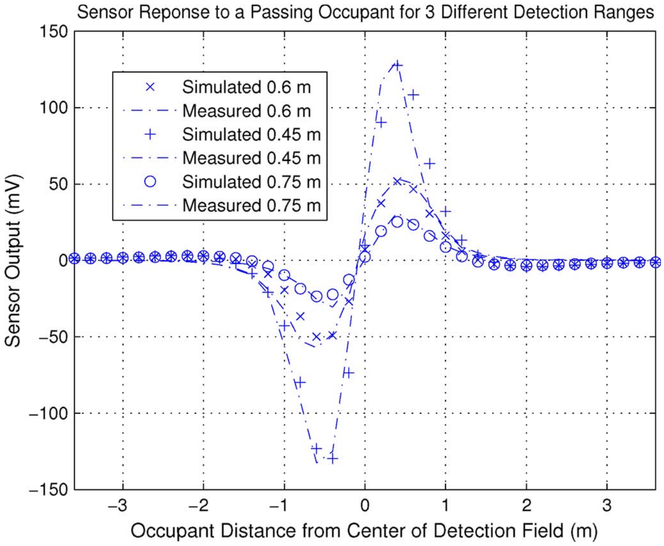

Fig. 15. Comparison between simulated and measured occupancy sensor output data.

F. Model Evaluation

Fig. 15 shows three comparisons between measured data taken from the lamp sensor and simulated data taken from the circuit in Fig. 16. The three plots in Fig. 15 correspond to three different lamp heights, 2.28 m, 2.43 m, and 2.58 m measured between the floor and the bottom of the bulb surfaces in the experimental setup. They show good agreement among the simulated and experimental data.

The system model in this section was presented "as-is" with little or no simplification. That is, the intent was to include all of the capacitances between all of the conducting nodes in the system as a starting point for a working model. Undoubtedly, accurate prediction is possible without considering all of those capacitances. Moreover, the simulation likely discounts some capacitances that may influence the sensor response. Finally, the limitations of the lumped-element capacitive model described in Section II-D should be considered when evaluating the model presented here.

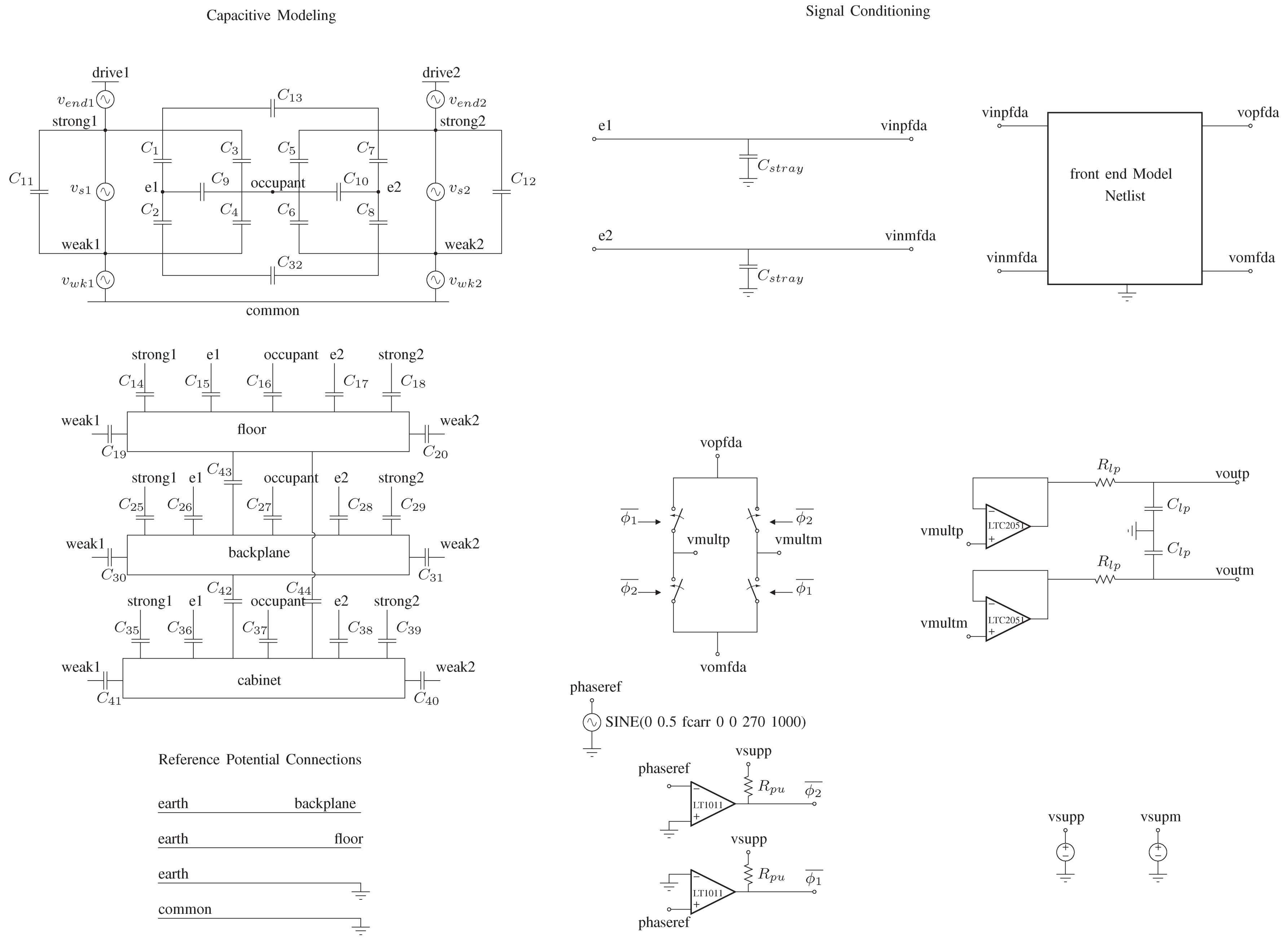

Fig. 16. SPICE simulation of the capacitive model, FD transimpedance amplifier front end and the signal conditioning electronics.

V. CONCLUSION

The modeling concepts that guide the design of a practical lamp sensor have been developed significantly in this paper. A new analytical circuit model of the fully-differential current-mode front end amplifier coupled with a lumped element capacitive model of the sensor system yielded a full system model. That model was validated against experimental data showing good agreement and verifying our understanding of the lamp sensor operating principles. Meanwhile, the full system model is useful in its own right because it may be used to study the effect of different lamp and electrode configurations, parasitic or stray capacitances, or other changes in the conducting environment below the lamp. The analysis and design of the lamp sensor electronics was expanded in Section III regarding frequency compensation of the current-mode front end amplifier and noise analysis of the signal conditioning system.

The development of the retrofit system presented here highlighted key modeling concepts and design techniques that enable useful implementations of capacitive occupancy sensors. By sensing electrostatic fields rather than IR, capacitive sensors enable true presence detection. Performance improvements of the lamp sensor are the subject of on going investigations. New embodiments of capacitive sensing occupancy detectors including stand-alone units and other retrofit systems are also the subject of further work. Finally, practical considerations like methods and frequency of calibration, e.g., to contend with rearrangement of fixed conducting objects, and their implications on use case scenarios are the topic of ongoing research.

REFERENCES

[1] *The Smart Grid: An Introduction*, U.S.D. of Energy, Aug. 2009. [Online]. Available: http://www.oe.energy.gov/1165.htm

[2] *Annual Energy Outlook 2010 Tables a4 and a5*, Energy Information Administration, U.D. Energy, Washington, DC, Feb. 2010.

[3] W. Yan, S. Hui, and H.-H. Chung, "Energy saving of large-scale high-intensity-discharge lamp lighting networks using a central reactive power control system," *IEEE Trans. Ind. Electron.*, vol. 56, no. 8, pp. 3069–3078, Aug. 2009.

[4] E. Bueno, A. Hernandez, F. Rodriguez, C. Giron, R. Mateos, and S. Cobreces, "A DSP- and FPGA-based industrial control with high-speed communication interfaces for grid converters applied to distributed power generation systems," *IEEE Trans. Ind. Electron.*, vol. 56, no. 3, pp. 654–669, Mar. 2009.

[5] A. Timbus, M. Larsson, and C. Yuen, "Active management of distributed energy resources using standardized communications and modern information technologies," *IEEE Trans. Ind. Electron.*, vol. 56, no. 10, pp. 4029–4037, Oct. 2009.

[6] J. Cooley, A.-T. Avestruz, and S. Leeb, "An autonomous distributed demand-side energy management network using fluorescent lamp sensors," in *Proc. IEEE PESC*, Jun. 2008, pp. 3907–3916.

[7] C. S. Moo, K. H. Lee, H. L. Cheng, and W. M. Chen, "A single-stage high-power-factor electronic ballast with ZVS buck–boost conversion," *IEEE Trans. Ind. Electron.*, vol. 56, no. 4, pp. 1136–1146, Apr. 2009.

[8] R. Orletti, M. Co, D. Simonetti, and J. de Freitas Vieira, "HID lamp electronic ballast with reduced component number," *IEEE Trans. Ind. Electron.*, vol. 56, no. 3, pp. 718–725, Mar. 2009.

[9] T.-E. Jang, H.-J. Kim, and H. Kim, "Dimming control characteristics of electrodeless fluorescent lamps," *IEEE Trans. Ind. Electron.*, vol. 56, no. 1, pp. 93–100, Jan. 2009.

[10] C.-S. Moo, C.-K. Huang, K.-H. Lee, and D.-J. Huang, "Repeatedly resonating ignition circuit for HID lamp electronic ballasts," *IEEE Trans. Ind. Electron.*, vol. 58, no. 1, pp. 244–249, Jan. 2011.

[11] J.-C. Hsieh and J. Lin, "Novel single-stage self-oscillating dimmable electronic ballast with high power factor correction," *IEEE Trans. Ind. Electron.*, vol. 58, no. 1, pp. 250–262, Jan. 2011.

[12] L. R. Center, "Investigation of the effects of dimming on fluorescent lamp life," Rensselaer Polytechnic Institute, Troy, NY, Tech. Rep., 2010.

[13] P. Zappi, E. Farella, and L. Benini, "Enhancing the spatial resolution of presence detection in a PIR based wireless surveillance network," in *Proc. IEEE Conf. AVSS*, Sep. 2007, pp. 295–300.

[14] Z. Zhang, X. Gao, J. Biswas, and J. K. Wu, "Moving targets detection and localization in passive infrared sensor networks," in *Proc. 10th Int. Conf. Inf. Fusion*, Jul. 2007, pp. 1–6.

[15] H. H. Kim, K. N. Ha, S. Lee, and K. C. Lee, "Resident location-recognition algorithm using a bayesian classifier in the pir sensor-based indoor location-aware system," *IEEE Trans. Syst., Man, Cybern. C, Appl. Rev.*, vol. 39, no. 2, pp. 240–245, Mar. 2009.

[16] W. Buller and B. Wilson, "Measurement and modeling mutual capacitance of electrical wiring and humans," *IEEE Trans. Instrum. Meas.*, vol. 55, no. 5, pp. 1519–1522, Oct. 2006.

[17] J. J. Cooley, "Capacitive sensing with a fluorescent lamp," M.S. thesis, MIT, Cambridge, 2007.

[18] J. Cooley, A.-T. Avestruz, and S. Leeb, "Proximity detection and ranging using a modified fluorescent lamp for security applications," in *Proc. 40th Annu. IEEE Int. Carnahan Conf. Security Technol.*, Oct. 2006, pp. 1–8.

[19] J. Cooley, A.-T. Avestruz, and S. Leeb, "A modified fluorescent lamp for discreet biometric surveillance," in *Proc. IEEE Conf. Technol. Homeland Security*, May 2007, pp. 227–233.

[20] J. Cooley, A.-T. Avestruz, S. Leeb, and L. Norford, "A fluorescent lamp with integral proximity sensor for building energy management," in *Proc. IEEE Power Electron. Spec. Conf.*, Jun. 2007, pp. 1157–1163.

[21] J. Smith, "Field mice: Extracting hand geometry from electric field measurements," *IBM Syst. J.*, vol. 35, no. 3.4, pp. 587–608, 1996.

[22] O. Fujiwara and T. Ikawa, "Numerical calculation of human-body capacitance by surface charge method," *Electron. Commun. Jpn.*, vol. 85, no. 12, pp. 38–44, Dec. 2002.

[23] B. George, H. Zangl, T. Bretterklieber, and G. Brasseur, "A novel seat occupancy detection system based on capacitive sensing," in *Proc. IEEE IMTC*, May 2008, pp. 1515–1519.

[24] E. Deng and S. Cuk, "Negative incremental impedance and stability of fluorescent lamps," in *Proc. 12th Annu APEC*, Feb. 1997, vol. 2, pp. 1050–1056.

[25] J. J. Cooley, "Analysis, modeling and design of energy management and multisource power systems," Ph.D. dissertation, MIT, Cambridge, May, 2010.

[26] L. T. Corp., Ltc2440 Datasheet, 2002.

[27] J. K. Roberge, *Operational Amplifiers: Theory and Practice*. Hoboken, NJ: Wiley, 1975.

[28] K. Nabors and J. White, "Multipole-accelerated capacitance extraction algorithms for 3-d structures with multiple dielectrics," *IEEE Trans. Circuits Syst. I, Fundam. Theory Appl.*, vol. 39, no. 11, pp. 946–954, Nov. 1992.

John J. Cooley (S'05) received the B.S. in electrical engineering, B.S. in physics, M.Eng., E.E., and Ph.D. degrees from Massachusetts Institute of Technology (MIT), Cambridge, in 2005, 2005, 2007, 2009, and 2011, respectively.

His interests are in electronics for building energy management and multisource power systems. He is currently with FastCAP Systems Inc., Boston, MA, where he is engaged in the design of power systems for advanced energy storage technologies in automotive and grid-level applications.

Al-Thaddeus Avestruz (M'04) received the B.S. degree in physics and the M.S. and E.E. degrees from Massachusetts Institute of Technology (MIT), Cambridge, in 1994 and 2006, respectively, where he is currently working toward the Ph.D. degree in electrical engineering at the Laboratory for Electromagnetic and Electronic Systems.

He was with several companies, including Teradyne Corporation, North Reading, MA, Thornton, Inc. (presently Mettler-Toledo Thornton, Capitol Heights, MD), and Diversified Technologies, Inc., Augusta, GA, before returning to MIT. His current research interests include circuit design, power conversion, energy, and electromagnetic systems.

Steven B. Leeb (F'07) received the Ph.D. degree in electrical engineering and computer science from Massachusetts Institute of Technology (MIT), Cambridge, in 1993.

He has been with the Department of Electrical Engineering and Computer Science, MIT, since 1993. He is currently a Professor at the Laboratory for Electromagnetic and Electronic Systems, MIT, where he is engaged in the design, analysis, development, and maintenance processes for all kinds of machinery with electrical actuators, sensors, or power electronic drives.